

# Solution-Processable, Low-Voltage, and High-Performance Monolayer Field-Effect Transistors with Aqueous Stability and High Sensitivity

Hongliang Chen, Shaohua Dong, Meilin Bai, Nongyi Cheng, Hao Wang, Mingliang Li, Huiwen Du, Shuxin Hu, Yanlian Yang, Tieying Yang, Fan Zhang, Lin Gu, Sheng Meng, Shimin Hou, and Xuefeng Guo\*

In general, carrier transport through the conductive channel of organic field-effect transistors (OFETs) occurs in, at most, the first few layers in the semiconductor at the dielectric/semiconductor interface.<sup>[1]</sup> This suggests that a densely packed defect-free two-dimensional (2D) crystalline semiconducting monolayer should exhibit a bulk-like carrier mobility and current modulation.<sup>[2]</sup> These types of monolayer field-effect transistors (MFETs) offer a model system that enables direct probing of the sensitivity of charge transport to various factors including molecular packing, film morphology, and temperature to better understand the intrinsic conduction mechanism.<sup>[3]</sup> Another unique feature of monolayer transistors is their two-dimensional nature, which maximizes the surface-to-volume ratio. A small change in the environment can lead to drastic changes in device characteristics, forming the basis for ultrasensitive sensing applications.<sup>[4]</sup>

To date there have been several reports that detail the development of MFETs by different approaches, including Langmuir–Blodgett (LB),<sup>[4b,5]</sup> self-assembly,<sup>[6]</sup> conductance-controlled evaporation,<sup>[7]</sup> and the coating technique.<sup>[8]</sup> However, the

realization of functional high-performance monolayer transistors for sensing applications remains a formidable challenge. Scaling the active semiconducting layers down to a monolayer confines the charge transport to two dimensions. Any structural imperfections, such as point defects or grain boundaries, result in deterioration of the charge transport. Therefore, the first prerequisite for efficient charge transport in MFETs is a highly ordered and defect-free crystalline semiconducting monolayer. Another issue is the nature of the electrode/semiconductor contact interface. Historically, establishing Ohmic contacts between electrodes and semiconductors has been challenging.<sup>[3a]</sup> Both the lack of long-range intermolecular  $\pi$ – $\pi$  coupling and the high injection barrier cause a reduction of the charge-carrier mobilities in monolayer transistors, normally orders of magnitude lower than those in the corresponding bulk thin film transistors.<sup>[7,9]</sup> In addition, for practical sensing applications, the device reliability and long-term operational stability, in particular in an aqueous detection environment, are serious problems that have to be solved.<sup>[10]</sup> To find solutions for these challenges, the device fabrication should be considered as a holistic process. The semiconductor materials, contact interface, and device engineering are so closely interrelated that they cannot be optimized independently. Herein, we described the design of a core-cladding liquid-crystalline pentathiophene for use in low-cost, low-voltage, and high-performance MFETs with solution-processed sol–gel HfO<sub>2</sub> thin films as nanoscale gate dielectrics (Figure 1a,b). Because the completely exposed monolayers support resistance-free contacts at the electrode/semiconductor interface and enforce one-dimensional conductivity, these monolayer devices are sensitive to external stimulus such as light and function as reporters to transduce analyte binding events into electrical signals with long-term operational stability and ultrahigh sensitivity, potentially enabling a new generation of ultrasensitive environmental and molecular sensors.

$\alpha$ -Substituted pentathiophene was used as the backbone of organic semiconductors (OSCs) (Figure 1a and Scheme S1, Supporting Information). We modified the pentathiophene core with strategically placed double-sided long alkyl chains for several design reasons. The first was to incorporate the self-assembling capabilities of liquid crystals into oligothiophene backbones. This enabled the molecules to spontaneously self-organize and optimize their highly ordered anisotropic packing during a thermal annealing treatment.<sup>[11]</sup> Second, it is well known that aliphatic chains increase the solubility of OSCs, thus improving their solution processability. These two considerations allow

H. Chen, Dr. S. Dong, N. Cheng, M. Li, Prof. X. Guo  
Center for Nanochemistry  
Beijing National Laboratory for Molecular Sciences  
State Key Laboratory for Structural  
Chemistry of Unstable and Stable Species  
College of Chemistry and Molecular Engineering  
Peking University  
Beijing 100871, PR China  
E-mail: guoxf@pku.edu.cn

M. Bai, H. Wang, Prof. S. Hou  
Key Laboratory for the Physics and Chemistry of Nanodevices  
Department of Electronics  
Peking University  
Beijing 100871, PR China

H. Du, Prof. Y. Yang  
National Center for Nanoscience and Technology  
Beijing 100190, PR China

Prof. S. Hu, F. Zhang, Prof. L. Gu, Prof. S. Meng  
Institute of Physics  
Chinese Academy of Sciences  
Beijing 100190, PR China

Prof. T. Yang  
Shanghai Institute of Applied Physics  
Chinese Academy of Sciences  
Shanghai 201204, PR China



DOI: 10.1002/adma.201405378

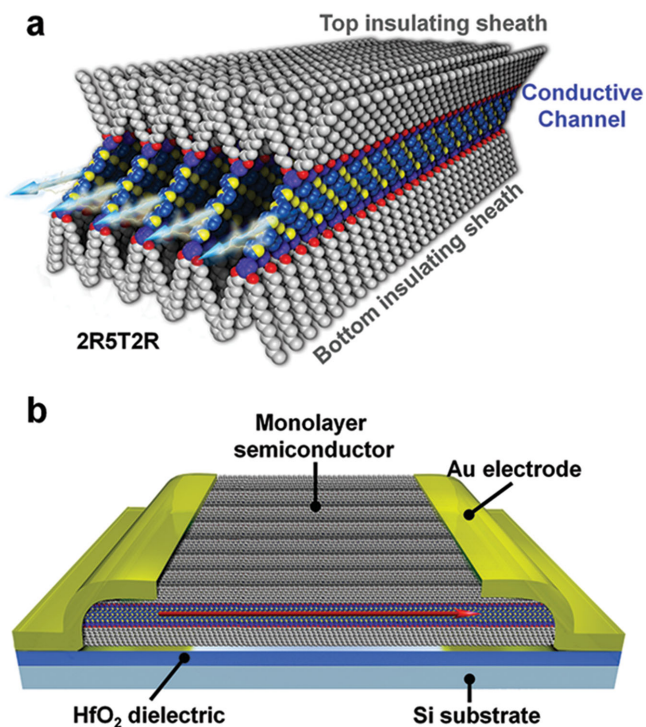


**Figure 1.** Schematic of an MFET. a) Molecular packing of the core-cladding liquid-crystalline pentathiophene (2R5T2R, see the Supporting Information). b) Schematic cross section of a solution-processed MFET.

for the high-yield and low-cost formation of high-quality monolayers by spin-coating. Third, two  $C_{12}$ -alkoxyphenyl groups were employed on each side of the molecules with specific purposes. The top two  $C_{12}$ -alkoxyphenyl groups made the surface hydrophobic, keeping the inner conductive core intact when the monolayer was in direct contact with aqueous environments. This design is crucial for achieving long-term resistance to water. Currently, only few organic materials have been confirmed to be stable when directly exposed to water.<sup>[12]</sup> Conversely, the bottom two  $C_{12}$ -alkoxyphenyl groups formed a passivating layer that eliminated the scattering/trapping sites from the dielectric surface. Usually octadecyltrichlorosilane (OTS)<sup>[13]</sup> or *n*-octadecylphosphonic acid (ODPA)<sup>[14]</sup> is used to modify the oxide dielectric surfaces to reduce the surface traps and tune the surface roughness. This design also offers the conformational degree of freedom, allowing molecules to overcome the rough surface and thus optimize their  $\pi$ - $\pi$  stacking. Collectively, these outer alkoxyphenyl-cladding layers provide a separate insulating sheath on each side that confines the charge carriers to a one-dimensional (1D) path (Figure 1a). This concept is important to optimize the optoelectronic properties of MFETs by maximizing the charge transport and separation.<sup>[15]</sup>

To date, MFETs reported in the literature have not been used in aqueous or marine environments because of the susceptibility of the OSCs to water and the high operating voltages. The former issue can be overcome by choosing appropriate OSCs with rational designs as discussed above. To achieve long-term operational stability in the presence of water, low-voltage device operation is necessary to avoid redox reactions that involve water and high ionic conduction through the analyte

solution.<sup>[10]</sup> Apart from this, low-power consumption is another attractive advantage for low-voltage device operation. This can be achieved by decreasing the dielectric thickness ( $d$ ) and/or increasing the dielectric constant ( $k$ ). Among many dielectrics (ref.<sup>[14b]</sup> and references therein), sol-gel  $HfO_2$  thin films are particularly appealing because of the simplicity of their solution processability, and their smooth and pinhole-free surface.<sup>[14a]</sup>

The synthesis of the semiconducting molecule (2R5T2R), the fabrication of sol-gel-processed ultrathin high- $k$   $HfO_2$  gate dielectrics, and the formation of the water-stable monolayer are detailed in the Supporting Information (Figure S1–S4, Supporting Information). To determine the structure of the monolayer, X-ray reflectivity (XRR) experiments were performed on an  $HfO_2$  surface. Figure 2a shows the reflectivity versus  $q_z$  with the corresponding fit for 2R5T2R. The scattering length density (SLD) profile (with  $SLD = \rho_e r_e$ , where  $\rho_e$  is the electron density and  $r_e$  represents the classical electron radius) provides further evidence of the homogeneous assembly of the monolayer (Figure 2b), which was modeled as a three-layer structure with different electron densities (Figure 2c,d).<sup>[16]</sup> From the surface normal SLD profile, the dedicated distributions of the top ( $SLD = 7.86 \times 10^{-6} \text{ \AA}^{-2}$ ) and bottom ( $SLD = 7.43 \times 10^{-6} \text{ \AA}^{-2}$ ) insulating  $C_{12}$ -alkyl chains were obtained, which were 12.9 and 14.2 Å thick, respectively. There was a pronounced region of higher SLD ( $SLD = 16.2 \times 10^{-6} \text{ \AA}^{-2}$ ), 22.1 Å thick, which was attributed to the oligothiophene  $\pi$ -system (Table S1, Supporting Information). This analysis yielded a monolayer thickness of  $\approx 4.9$  nm, which is consistent with the AFM measurements (Figure S2i, Supporting Information). Compared with the molecular lengths ( $\approx 15.5$  Å for the alkyl chain with a fully extended conformation and  $\approx 28.6$  Å for the oligothiophene backbone), these values suggest that both the planes, where the two alkyl chains were separate, placed on the top and bottom of the oligothiophene backbone (with different angles induced by the substrate effects:  $\approx 67^\circ$  for the top and  $\approx 47^\circ$  for the bottom) and, were almost perpendicular to the substrate. The oligothiophene backbone, sandwiched between the top and bottom insulating layers, was oriented at an angle of inclination of  $\approx 50^\circ$  relative to the substrate (Figure 2c,d).<sup>[6a,c]</sup> This orientation is consistent with the solid-state UV-vis measurements that revealed a *J*-type aggregation that had all-*anti* conformations in the monolayers (Figure S3e,f, Supporting Information).<sup>[17]</sup>

Synchrotron grazing-incidence X-ray diffraction (GIXD) measurements were performed to probe the long-range in-plane order in both a partially covered monolayer and a multilayer obtained from solutions with different concentrations (Figure 2e). The diffracted intensity is presented as a color map in Figure 2f as a function of out-of-plane and in-plane scattering vectors,  $q_z$  and  $q_{xy}$ , respectively. The vertical lines are the so-called Bragg rods, originating from the absence of periodicity perpendicular to the ordered layer. This observation demonstrates the in-plane order arising from the thiophene units. The in-plane projections of Figure 2f are shown in Figure 2g. The (10) and (01) peaks are absent, while (11) and (12) exist, which is indicative of a  $p2gg$  symmetry in the  $a$ - $b$  plane with a herringbone arrangement of the two molecules. The diffraction pattern represents a rectangular in-plane unit cell with dimensions  $a = 7.36$  Å,  $b = 8.62$  Å, and  $\gamma = 90^\circ$ . In addition, Bragg reflections in the monolayer diffraction pattern (Figure 2g top)

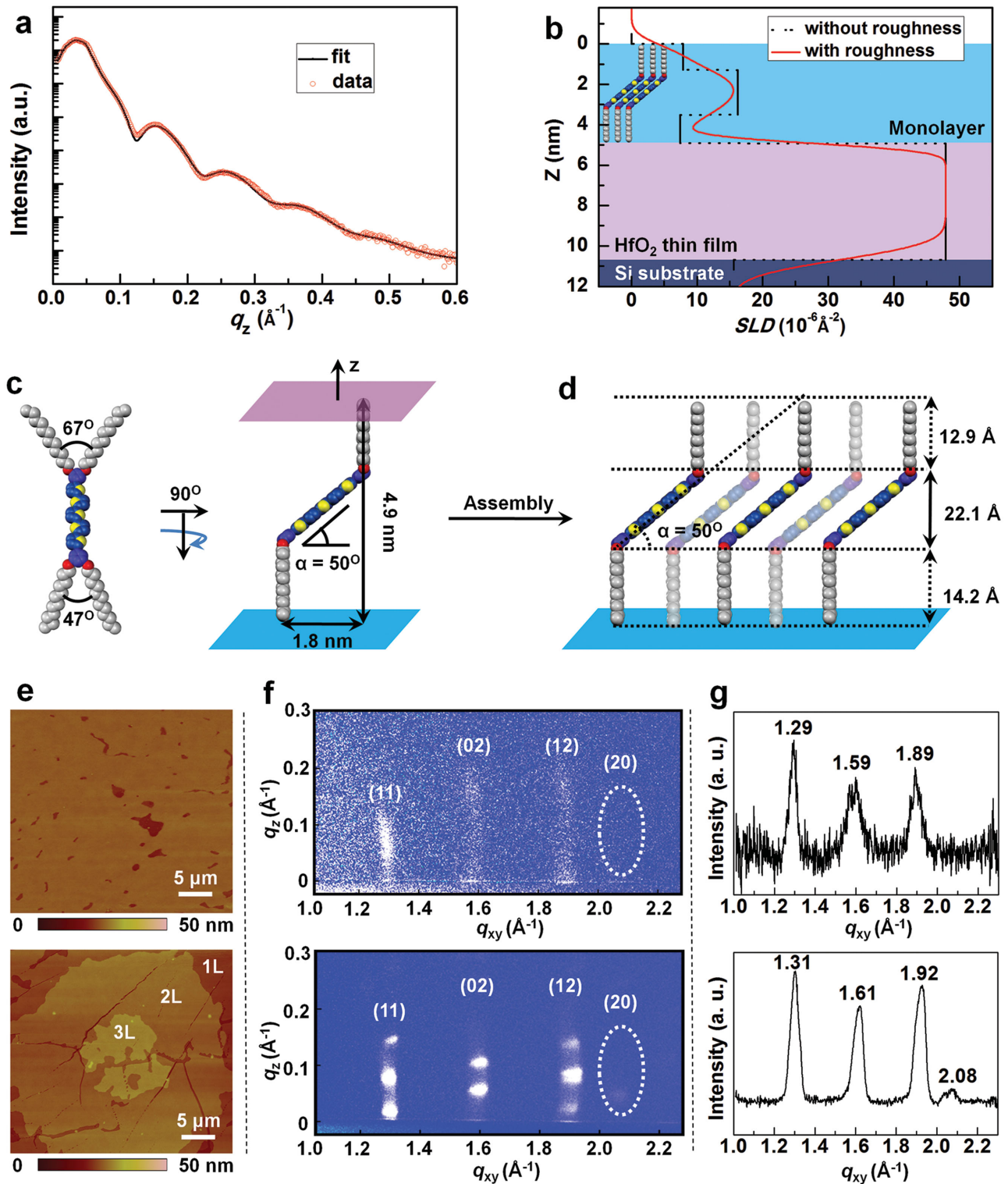


**Figure 2.** Characterization of the monolayer microstructure. a) XRR measurement (dots) of the monolayer with an HfO<sub>2</sub> thin film on a silicon substrate and the corresponding fit (solid line). b) SLD profile with (solid line) and without (dashed line) roughness. c) Space-filling model of a reasonable conformation of 2R5T2R. d) Schematic interpretation of a monolayer on the HfO<sub>2</sub> surface, illustrating the three-layer packing model in the monolayer. e) AFM images showing the morphologies of the sub-monolayer (95% coverage of the monolayer, top) and the three-layer film ( $\approx 15$  nm thick, bottom) used for the GIXD measurements. f) Diffraction patterns for a monolayer (top) and a three-layer film (bottom) on SiO<sub>2</sub>, showing the presence of Bragg rods. g) The corresponding integrated intensity in the diffraction pattern as a function of  $q_{xy}$ .

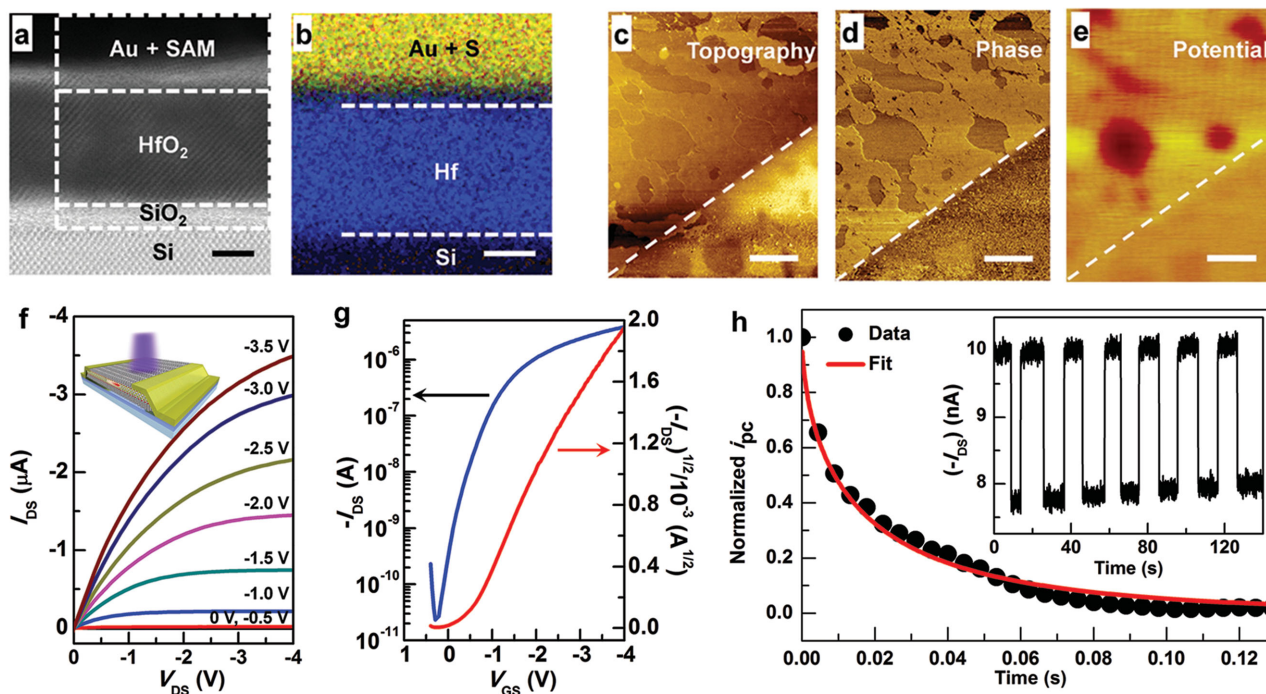


**Figure 3.** Optoelectronic properties of MFETs. a,b) Cross-sectional STEM images of a monolayer. The sample was prepared using a focused ion beam and imaged by STEM (200 kV). The scale bar is 2 nm. c–e) SKPM measurements of a partially covered MFET: the topography (c), phase (d), and surface potential (e). The scale bar is 1  $\mu\text{m}$ . f) Output characteristics of an MFET.  $L = 300$  and  $W = 500$   $\mu\text{m}$ . The inset shows the schematic of the MFET used for the photoresponsive measurements. The gate voltage ( $V_{\text{GS}}$ ) ranged from 0 to  $-3.5$  V in  $-0.5$  V steps. g) Transfer characteristics with the source–drain voltage ( $V_{\text{DS}}$ ) =  $-4$  V. h) Normalized decay curve, fitted with a stretched exponential. This curve was extracted by averaging the photocurrent decays of the MFET as a function of time using 450-nm monochromatic light (inset) ( $I_{\text{light}} = 0.15$   $\text{mW cm}^{-2}$ ).  $L = 50$  and  $W = 150$   $\mu\text{m}$ .  $V_{\text{GS}} = -2$  V and  $V_{\text{DS}} = -2$  V.

were comparable with those in the multilayer pattern (Figure 2g bottom), indicating that the 2D lattice of both the monolayer and the thick film had very similar crystalline structures.<sup>[7]</sup> In comparison with the multilayer case (Figure 2g bottom), the intensity of the (20) peak in the monolayer was too weak to observe (Figure 2g top). In conjunction with scanning tunneling microscopy (STM) studies (Figure S5, Supporting Information), the GIXD measurements indicated that the solution-processed monolayer was a densely packed, smooth monolayer.

To uncover the structure of the electrode/semiconductor interface, images were taken of the critical region where the monolayer was connected to gold electrodes, by cross-sectional scanning transmission electron microscopy (STEM). The visualization of the layer structure is realized using the double-spherical-aberration-corrected STEM with a spatial resolution of  $\approx 0.80$   $\text{\AA}$  (Figure 3a and Figure S6a, Supporting Information). The device had the following architecture: silicon substrate/ $\text{HfO}_2$  gate dielectric/monolayer/gold layer/protecting platinum layer. Clearly imaging the interface between the monolayer and the gold layer was difficult. Therefore, the elemental compositions of the individual layers were analyzed using an energy-dispersive X-ray system (EDX). The presence of carbon, oxygen and sulfur (Figure S6b–d, Supporting Information), which are the fingerprints of the molecules in the monolayer, confirmed the formation of a monolayer. Figure 3b shows the combined RGB map, where sulfur is presented in orange (Figure S6d,

Supporting Information) and gold is in purple (Figure S6e, Supporting Information). It was clear that gold atoms diffused into the monolayer. This was attributed to the formation of Au–S bonds, which are commonly used to polish the electrode surface in OFETs.<sup>[18]</sup> Further X-ray photoelectron spectroscopic (XPS) measurements also confirmed the formation of Au–S bonds (Figure S7, Supporting Information). Considering the fact that the HOMO energy level matched the work function of gold, the Au–S bond formation directly produced the intimate electrical contact without a Schottky barrier.

To further probe the contact interface, scanning Kelvin probe microscopy (SKPM) measurements were applied to partially covered MFETs. The topography and phase images of a partially covered MFET are presented in Figure 3c,d, showing obvious grain boundaries in the monolayer. The local potential was determined using SKPM with grounded electrodes and  $-3$  V applied to the gate. Figure 3e shows the corresponding spatially resolved potential map. In comparison with the topography and phase images, the surface potential was smooth without steps either at the grain boundaries or at the Au/monolayer interface. The absence of steps demonstrates that the monolayer had a homogeneous conductivity and more importantly, the contact resistance is nearly negligible, which is consistent with the cross-sectional STEM experiments. The long-range tight packing of the monolayer molecules and barrier-free Au/monolayer contacts are essential for the useful optoelectronic properties described below.

Having understood the structure of the monolayer and the nature of the contact, we then explored the optoelectronic properties of MFETs using a bottom-gate top-contact device architecture (Figure 1b). Typical output and transfer characteristics for an MFET with the interdigitated electrodes (channel length ( $L$ ): 300  $\mu\text{m}$  and channel width ( $W$ ): 500  $\mu\text{m}$ ) are presented in Figure 3f,g. All of the MFETs had stable operation in ambient air at low voltages (less than  $-4.0$  V) (Figure S8, Supporting Information). An average mobility of  $\approx 8.0 \times 10^{-2} \text{ cm}^2 \text{ V}^{-1} \text{ s}^{-1}$  and an average on/off ratio on the order of  $10^5$  were achieved based in over 100 individual devices. These values are comparable with traditional thin film transistors (semiconductor layer  $\approx 50$  nm thick) fabricated on OTS-modified  $\text{SiO}_2$  surface and ranked the highest among monolayer-based FETs.<sup>[2,3]</sup>

The MFETs were light sensitive. The DC photoconductivity was measured at room temperature in ambient atmosphere under light illumination (Figure S9, Supporting Information). Figure S9c (Supporting Information) shows the power-dependent photocurrent of an MFET with a linear relationship. This finding is surprising and rare because the photocurrent in the devices occurs in a single 4.9 nm-thick layer (2.2 nm in an oligothiophene  $\pi$ -system).<sup>[4b]</sup> This was attributed to efficient separation and transport of the photoexcited electron-hole pairs caused by the unique synergistic effects of the Ohmic Au/monolayer contacts and the alkyl chain-protected conducting path. The separated electrons can also be trapped at the semiconductor/dielectric interface that induces the shift of the threshold voltage to more positive direction (Figure S9a, Supporting Information). To understand the role of the monolayer on the device photoconductivity, wavelength-dependent measurements were carried out. The calculated responsivities are shown in Figure S9d (Supporting Information) as a function of wavelength. The peaks in the responsivity spectrum match those in the UV-vis absorption spectrum, indicating the key role of the monolayers in the device characteristics. The maximum responsivity reported here is the first and is moderate,  $\approx 0.4 \text{ A W}^{-1}$ , leaving plenty of room for further improvement.

To further examine the confined photoconductivity mechanism, the photocurrent decay dynamics were measured by a lock-in amplifier after the device was illuminated. Figure 3h (inset) shows several reproducible cycles of the stable photocurrents when the 450 nm monochromatic light was switched on and off. The decay time was fast (less than 0.1 s) (Figure 3h). The decay curves were fitted to the stretched exponential:

$$i_{\text{pc}}(t) = i_0 \exp[-(t/\tau)^\beta] \quad 0 < \beta < 1$$

where  $i_{\text{pc}}$  is the photocurrent and  $\tau$  is the carrier lifetime. This equation is referred to as the Williams–Watts function<sup>[19]</sup> and in general describes the relaxation of systems that are not at equilibrium.  $\beta$  is generally ascribed to the degree of dispersion in the decay kinetics.  $\beta = 1$  corresponds to no dispersion, while  $\beta < 1$  means that the dispersion increases as it approaches zero.<sup>[19b]</sup> This exponent has been connected to the dimensionality of the transport phenomena where in 3D systems  $\beta = 1$  and in 1D materials  $\beta = 0.5$ .<sup>[19c]</sup> By applying this analysis to the persistent photocurrent measurements of our MFETs, the averaged decay curves could be fitted with the Williams–Watts function using  $\beta = 0.55$  and  $\tau = 0.015$  s. This  $\beta$  value indicates

an exclusively enforced one-dimensional charge transport path, which is in agreement with our design and sets the foundation for the following sensing applications in water.

Figure 4a illustrates the device architecture, where a microfluidic channel was integrated into the MFET system for real-time measurements. To rule out potential artifacts from Schottky barrier modification between the analytes and metal electrodes, Au leads were passivated with a 50 nm-thick layer of  $\text{SiO}_2$  by electron beam evaporation before polydimethylsiloxane (PDMS) stamping. First, the stability of our MFETs under aqueous environments was tested, a feature that is critical for biosensing applications. Figure 4b shows a comparison of the transfer characteristics of an MFET measured under an atmospheric condition and in deionized (DI) water, after it was kept in DI water for 20 days. Remarkably, the device performance was similar to that observed under atmospheric conditions, with a minimal increase in the device's off-current and a slightly positive shift of the threshold voltage ( $V_T$ ). This was attributed to traps, caused by  $\text{H}_3\text{O}^+$  diffusing into the film.<sup>[12]</sup> The average electrical figures of merit were calculated for over 15 different devices (in ambient: mobility ( $\mu$ )  $\approx 0.08 \pm 0.01 \text{ cm}^2 \text{ V}^{-1} \text{ s}^{-1}$  and on/off  $\approx 10^5$ ; in DI water:  $\mu \approx 0.06 \pm 0.01 \text{ cm}^2 \text{ V}^{-1} \text{ s}^{-1}$  and on/off  $\approx 10^4$  (see Figure S10, Supporting Information)).

Then we demonstrated the device's capability of in situ detecting trace amounts of chemical species in aqueous solution, using melamine as a representative. The changes in the drain current of the MFETs were measured while melamine solutions with different concentrations were flowed into the PDMS channel through a syringe pump. All of the real-time electrical measurements were conducted at a constant bias voltage of  $-500$  mV and gate voltage of  $-500$  mV, unless otherwise mentioned. Figure 4c shows real-time electrical readouts for both bulk thin-film transistor-based (top) and MFET-based (bottom) sensors that were exposed to melamine solutions with concentrations ranging from 0.01 to 1000 ppm. It was obvious that the MFET device had an improved sensitivity, as low as 0.01 ppm, which is at least three orders of magnitude higher than that of bulk thin-film transistor sensors (10 ppm) and ranked the highest among all OFET-based sensors.<sup>[10]</sup> In addition, the average response time for each step was about 2 s, which is much faster than those in previous reports (minute level).<sup>[12a,c]</sup> A control experiment using the same MFET, in the absence of melamine, did not show any obvious changes in the current under the same conditions (Figure 4c, bottom). Because of the very low concentrations, the pH values we measured from solutions with different melamine concentrations ranged from 6.6 to 7.5 (22.1  $^\circ\text{C}$ ), which is equal to the error range of the DI water. These results ruled out the possibility that the current changes originated from either of water or pH changes. To obtain the calibration curve for melamine detection, the relative current change was plotted against the melamine concentration (Figure 4d). The responses scale for the logarithm of the melamine concentration spanned over five orders of magnitude (Figure 4d inset). Using a value three times the standard deviation (replicated over 10 times) of the response measured in the DI water reference as the minimum detection limit (MDL), the MDL were estimated to be  $\approx 0.01$  ppm for the MFETs, which was achieved experimentally. These results demonstrate that MFETs possess unique virtues in chemical and biological

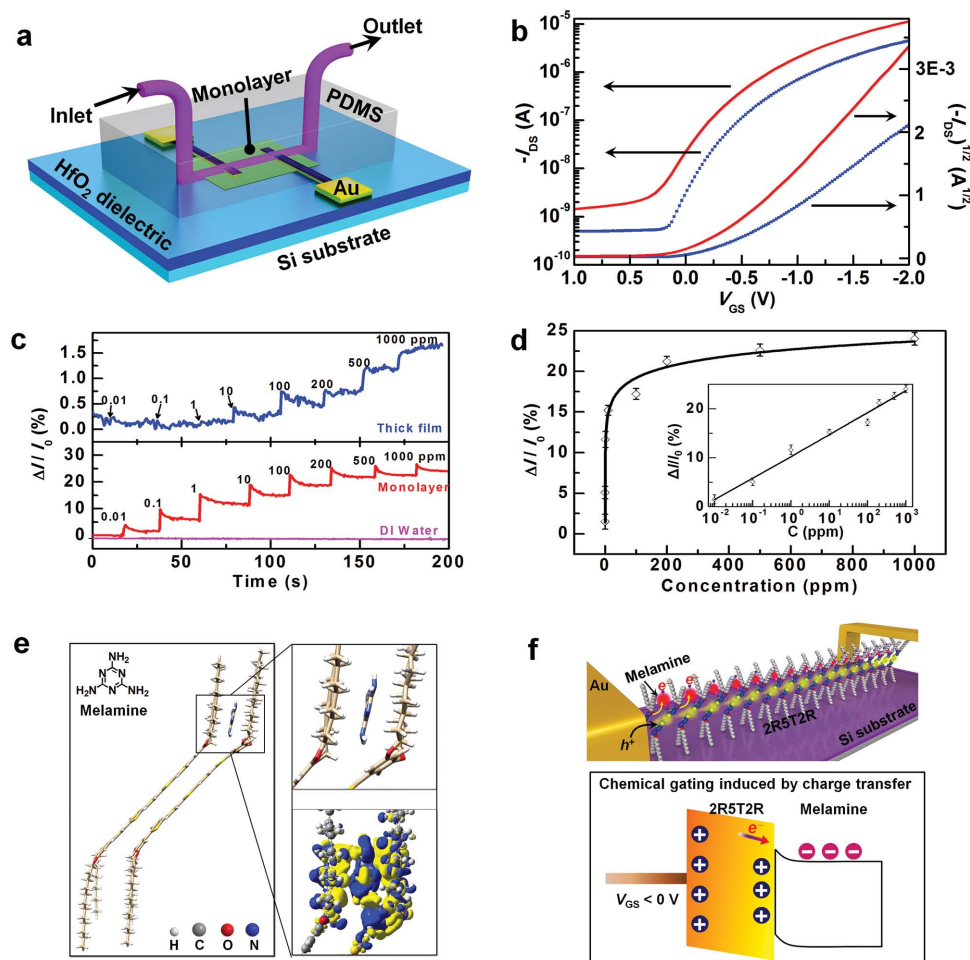


**Figure 4.** Real-time electrical detection of melamine in water. a) Schematic of an MFET with a microfluidic channel for real-time detection. The metal electrodes were passivated with 50 nm SiO<sub>2</sub> using electron beam evaporation (see the Supporting Information). b) Transfer characteristics in ambient air (blue) and DI water (red).  $V_{DS} = -2$  V. c) Real-time electrical measurements of MFETs with different concentrations of melamine. Top: a 50 nm-thick film (blue: melamine). Bottom: a monolayer (red: melamine magenta: DI water as the control).  $V_{DS} = -2$  V and  $V_{GS} = -2$  V. d) Calibration curve: relative change in the current versus melamine concentration (ppm). The inset shows the fitted curve on a natural logarithmic scale, showing an estimated MDL of  $\approx 10$  ppb. e) Cross-sectional views of the absorption geometries and the corresponding charge transfer density between melamine and 2R5T2Rs. The blue and yellow regions represent the maximum charge accumulation and maximum charge depletion, respectively. f) Schematic of the sensing mechanism (top) and the energy-level diagram for the 2R5T2R/melamine interface (bottom). Physical absorption induced electron transfer from 2R5T2R to melamine, leaving holes in the conductive channel that flowed toward the drain. The electrons remained in the melamine layer, resulting in a built-in electric field and then recirculating the positive charge carriers in the 2R5T2R channel.

sensors because of their inherent ultrasensitivity that arises from an active monolayer being exposed to the environment.

To better understand the sensing mechanism, the interactions between the melamine and 2R5T2R molecules were investigated by employing calculations using density functional theory. As the intermolecular interactions were mainly contributed by the nearest-neighboring molecules, a sensing model consisting of one melamine molecule and two 2R5T2R molecules was constructed (Figure 4e). The calculations showed that the melamine molecules preferred to stay between the alkyl groups with a binding energy of 0.65 eV, displaying an intimate contact with the pentathiophene cores while keeping the conducting channel intact. This provided the long-term sensing stability in the devices in water. To reveal the physical origin of the binding energy, the intermolecular charge transfer was

calculated. From the charge distribution between the melamine and 2R5T2R overlayer (Figure 4e), we found a partial charge of 0.13 electrons being transferred from the two 2R5T2R molecules to the melamine molecule. These calculations indicate the following model of the underlying physical mechanism of detection in the device (Figure 4f, top). Melamine absorption in the 2R5T2R monolayer produced electron transfer because of band bending at the melamine/2R5T2R interface, induced by the energy level misalignment at this interface (Figure 4f, down). This electron transfer left a positive charge (holes) in the conductive channel, leading to a carrier density increase in a p-type semiconductor (and thus an increase in conductance). As the transferred electrons remained trapped in the melamine layer, the negatively charged melamine molecules functioned as an additional gate and induced positive carriers in the 2R5T2R

monolayer through capacitive coupling. As long as the melamines remained negatively charged, positive charges in the 2R5T2R monolayer were recirculated, therefore resulting in an improved sensitivity. This chemo-gating effect is schematically shown in Figure 4f.

In this work, we designed a core-cladding liquid-crystalline pentathiophene OSC, where its conductive pentathiophene core was sandwiched by two insulating alkyl sheaths, enforcing the charge carrier transport to be exclusively one-dimensional along densely packed, long-range ordered  $\pi$ -conjugated columns. In conjunction with another important design that established the Ohmic contacts between the electrodes and semiconductors by the formation of Au–S bonds, this carrier transport confinement maximized the efficient charge generation and transport. By using solution-processed high- $k$  HfO<sub>2</sub> thin films as a nanoscale gate dielectric, these designs produced low-voltage, high-performance functional MFETs that were light-sensitive. More importantly, in combination with microfluidics, these devices displayed in situ detection of chemical and biological analytes with the long-term operational stability in water through a noninvasive sensing mechanism of charge transfer-induced capacitive coupling and ultrahigh sensitivity, which reached the minimum detection limit of MFETs ( $\approx 10$  ppb). The proven reliability and ability to integrate these MFET devices into traditional industrial technologies (such as complementary metal oxide semiconductor (CMOS)) have the potential to make low-cost, portable detection arrays and may provide a significant step toward practical electrical chemo-/biosensors.

## Supporting Information

Supporting Information is available from the Wiley Online Library or from the author.

## Acknowledgements

H.C. and S.D. contributed equally to this work. This work was supported by the National Natural Science Funds of China (Grant Nos. 21225311, 91333102, 21373014, and 51121091) and the 973 Project (Grant Nos. 2012CB921404 and 2013CB933404). The authors thank Prof. Lijun Wan and Dr. Bo Cui for help with the STM characterization.

Received: November 24, 2014

Revised: January 14, 2015

Published online: February 13, 2015

- [1] a) A. Dodabalapur, L. Torsi, H. E. Katz, *Science* **1995**, 268, 270; b) F. Dinelli, M. Murgia, P. Levy, M. Cavallini, F. Biscarini, D. M. de Leeuw, *Phys. Rev. Lett.* **2004**, 92, 196802.
- [2] a) M. Halik, A. Hirsch, *Adv. Mater.* **2011**, 23, 2689; b) H. Chen, X. Guo, *Small* **2013**, 9, 1144.
- [3] a) Y. Cao, M. L. Steigerwald, C. Nuckolls, X. Guo, *Adv. Mater.* **2010**, 22, 20; b) J. J. Brondijk, W. S. C. Roelofs, S. G. J. Mathijssen, A. Shehu, T. Cramer, F. Biscarini, P. W. M. Blom, D. M. de Leeuw, *Phys. Rev. Lett.* **2012**, 109, 056601.
- [4] a) A.-M. Andringa, M.-J. Spijkman, E. C. P. Smits, S. G. J. Mathijssen, P. A. van Hal, S. Setayesh, N. P. Willard, O. V. Borshchev, S. A. Ponomarenko, P. W. M. Blom, D. M. de Leeuw, *Org. Electron.* **2010**, 11, 895; b) Y. Cao, Z. Wei, S. Liu, L. Gan, X. Guo, W. Xu, M. L. Steigerwald, Z. Liu, D. Zhu, *Angew. Chem., Int. Ed.* **2010**, 49, 6319; c) X. Guo, M. Myers, S. Xiao, M. Lefenfeld, R. Steiner, G. S. Tulevski, J. Tang, J. Baumert, F. Leibfarth, J. T. Yardley, M. L. Steigerwald, P. Kim, C. Nuckolls, *Proc. Natl. Acad. Sci. USA* **2006**, 103, 11452.
- [5] S. Fabiano, C. Musumeci, Z. Chen, A. Scandurra, H. Wang, Y.-L. Loo, A. Facchetti, B. Pignataro, *Adv. Mater.* **2012**, 24, 951.
- [6] a) E. C. P. Smits, S. G. J. Mathijssen, P. A. van Hal, S. Setayesh, T. C. T. Geuns, K. A. H. A. Mutsaers, E. Cantatore, H. J. Wondergem, O. Werzer, R. Resel, M. Kemerink, S. Kirchmeyer, A. M. Muzafarov, S. A. Ponomarenko, B. de Boer, P. W. M. Blom, D. M. de Leeuw, *Nature* **2008**, 455, 956; b) S. G. J. Mathijssen, E. C. P. Smits, P. A. van Hal, H. J. Wondergem, S. A. Ponomarenko, A. Moser, R. Resel, P. A. Bobbert, M. Kemerink, R. A. J. Janssen, D. M. de Leeuw, *Nat. Nanotechnol.* **2009**, 4, 674; c) T. Schmaltz, A. Y. Amin, A. Khassanov, T. Meyer-Friedrichsen, H.-G. Steinrueck, A. Magerl, J. J. Segura, K. Voitchovsky, F. Stellacci, M. Halik, *Adv. Mater.* **2013**, 25, 4511; d) M. Novak, A. Ebel, T. Meyer-Friedrichsen, A. Jedaa, B. F. Vieweg, G. Yang, K. Voitchovsky, F. Stellacci, E. Spiecker, A. Hitsch, M. Halik, *Nano Lett.* **2011**, 11, 156; e) G. S. Tulevski, Q. Miao, M. Fukuto, R. Abram, B. Ocko, R. Pindak, M. L. Steigerwald, C. R. Kagan, C. Nuckolls, *J. Am. Chem. Soc.* **2004**, 126, 15048; f) C. M. Jaeger, T. Schmaltz, M. Novak, A. Khassanov, A. Vorobiev, M. Hennemann, A. Krause, H. Dietrich, D. Zahn, A. Hirsch, M. Halik, T. Clark, *J. Am. Chem. Soc.* **2013**, 135, 4893.
- [7] E. M. Mannebach, J. W. Spalenka, P. S. Johnson, Z. Cai, F. J. Himpfel, P. G. Evans, *Adv. Funct. Mater.* **2013**, 23, 554.
- [8] a) M. Defaux, F. Gholamrezaie, J. Wang, A. Kreyes, U. Ziener, D. V. Anokhin, D. A. Ivanov, A. Moser, A. Neuhold, I. Salzmann, R. Resel, D. M. de Leeuw, S. C. J. Meskers, M. Moeller, A. Mourran, *Adv. Mater.* **2012**, 24, 973; b) L. Jiang, H. Dong, Q. Meng, H. Li, M. He, Z. Wei, Y. He, W. Hu, *Adv. Mater.* **2011**, 23, 2059.
- [9] a) R. Ruiz, A. Papadimitratos, A. C. Mayer, G. G. Malliaras, *Adv. Mater.* **2005**, 17, 1795; b) S. C. B. Mannsfeld, A. Virkar, C. Reese, M. F. Toney, Z. Bao, *Adv. Mater.* **2009**, 21, 2294.
- [10] a) P. Lin, F. Yan, *Adv. Mater.* **2012**, 24, 34; b) P. A. Bobbert, A. Sharma, S. G. J. Mathijssen, M. Kemerink, D. M. de Leeuw, *Adv. Mater.* **2012**, 24, 1146; c) J. Mei, Y. Diao, A. L. Appleton, L. Fang, Z. Bao, *J. Am. Chem. Soc.* **2013**, 135, 6724.
- [11] a) S. Dong, H. Zhang, L. Yang, M. Bai, Y. Yao, H. Chen, L. Gan, T. Yang, H. Jiang, S. Hou, L. Wan, X. Guo, *Adv. Mater.* **2012**, 24, 5576; b) I. McCulloch, M. Heaney, C. Bailey, K. Genevicius, I. Macdonald, M. Shkunov, D. Sparrowe, S. Tierney, R. Wagner, W. M. Zhang, M. L. Chabinc, R. J. Kline, M. D. McGehee, M. F. Toney, *Nat. Mater.* **2006**, 5, 328; c) A. van Breemen, P. T. Herwig, C. H. T. Chlon, J. Sweelssen, H. F. M. Schoo, S. Setayesh, W. M. Hardeman, C. A. Martin, D. M. de Leeuw, J. J. P. Valetton, C. W. M. Bastiaansen, D. J. Broer, A. R. Popa-Merticaru, S. C. J. Meskers, *J. Am. Chem. Soc.* **2006**, 128, 2336.
- [12] a) M. E. Roberts, S. C. B. Mannsfeld, N. Queraltó, C. Reese, J. Locklin, W. Knoll, Z. Bao, *Proc. Natl. Acad. Sci. USA* **2008**, 105, 12134; b) D. A. Bernards, G. G. Malliaras, *Adv. Funct. Mater.* **2007**, 17, 3538; c) O. Knopfmacher, M. L. Hammock, A. L. Appleton, G. Schwartz, J. Mei, T. Lei, J. Pei, Z. Bao, *Nat. Commun.* **2014**, 5, 2954; d) T. Jung, A. Dodabalapur, *Appl. Phys. Lett.* **2005**, 87, 182109; e) B. Kang, M. Jang, Y. Chung, H. Kim, S. K. Kwak, J. H. Oh, K. Cho, *Nat. Commun.* **2014**, 5, 4752.
- [13] Y. Ito, A. A. Virkar, S. Mannsfeld, J. H. Oh, M. Toney, J. Locklin, Z. Bao, *J. Am. Chem. Soc.* **2009**, 131, 9396.
- [14] a) O. Acton, G. Ting, H. Ma, J. W. Ka, H.-L. Yip, N. M. Tucker, A. K. Y. Jen, *Adv. Mater.* **2008**, 20, 3697; b) R. P. Ortiz, A. Facchetti, T. J. Marks, *Chem. Rev.* **2010**, 110, 205.

- [15] Y. S. Cohen, S. Xiao, M. L. Steigerwald, C. Nuckolls, C. R. Kagan, *Nano Lett.* **2006**, *6*, 2838.
- [16] H. Zhang, X. Guo, J. Hui, S. Hu, W. Xu, D. Zhu, *Nano Lett.* **2011**, *11*, 4939.
- [17] L. Huang, M. Stolte, H. Bürckstümmer, F. Würthner, *Adv. Mater.* **2012**, *24*, 5750.
- [18] G. S. Tulevski, Q. Miao, A. Afzali, T. O. Graham, C. R. Kagan, C. Nuckolls, *J. Am. Chem. Soc.* **2006**, *128*, 1788.
- [19] a) G. Williams, D. C. Watts, *Trans. Faraday Soc.* **1970**, *66*, 80; b) J. M. Warman, P. G. Schouten, G. H. Gelinck, M. P. de Haas, *Chem. Phys.* **1996**, *212*, 183; c) M. F. Shlesinger, E. W. Montroll, *Proc. Natl. Acad. Sci. USA* **1984**, *81*, 1280.
-